Improving thermodynamic stability of nano-$LiMn_2O_4$ for Li-ion battery cathode

Kimiko Nakajima[1], Flavio L. Souza[2,3], Andre L.M. Freitas[2], Andrew Thron[1], Ricardo H. R. Castro[1,*]

[1]Department of Materials Science and Engineering, University of California, Davis, Davis, California 95616, United States

[2]Laboratory of Alternative Energy and Nanomaterials (LEAN), Universidade Federal do ABC, Santo André, Brazil

[3]Brazilian Nanotechnology National Laboratory (LNNano), Brazilian Center for Research in Energy and Materials (CNPEM), Campinas, Brazil

**Corresponding author: rhrcastro@ucdavis.edu*

Abstract

Nanomaterials can exhibit improved electrochemical performance in cathode applications, but their inherently high surface areas cause unconventional instability, leading to capacity fading after a limited number of battery cycles. This is because of their high surface reactivity which makes them more susceptible to phenomena such as grain growth, sintering, solubilization, and phase transformations. Thermodynamically, these can be attributed to increased contribution of interfacial enthalpies to the total free energy of the system. The lack of experimental \ data on interfacial thermodynamics of lithium-based materials has hindered strategies to mitigate such degradation mechanisms. In this study, interfacial energies of $LiMn_2O_4$ nanoparticles were directly measured for the first time using calorimetry, and the possibility of thermodynamically manipulating both surface and grain boundary energies using a dopant (scandium) was explored. We show that undoped $LiMn_2O_4$ nanoparticles have a surface energy of 0.85 J/m^2 which is significantly lower than that of $LiCoO_2$. Moreover, introducing scandium further lowered

$LiMn_2O_4$ surface energy, leading to demonstrated improved stability against coarsening and reactivity to water, which can potentially reflect in more stable cathode materials for battery applications.

Introduction

$LiMn_2O_4$ (LMO) finds application as cathode material for Li-ion battery as an alternative to $LiCoO_2$, which shows significant drawbacks related to instability. Although LMO has its own disadvantages, its application in the form of *nanostructured* cathodes has been shown effective in enhanced Li^+ transport due to its increased electrode to electrolyte contact area.[1–5] However, capacity fading after extended cycling is still a challenge, which is largely associated with the intrinsic chemical and structural instability exacerbated at the nanoscale.[2,4,6] These instabilities include dissolution of Mn ions from the surface, Jahn-Teller distortion of LMO spinel structure, and mechanical failures initiated by intergranular cracking, which affect Li^+ mobility and reversibility of charge/discharge reactions.[7–12]

In general, at the nanoscale, properties and processes, such as fracture toughness, reactivity, phase transitions, and coarsening, are strongly dependent on interfacial characteristics.[13–21] In particular, interfacial energies, which include both solid-vapor (surface) and solid-solid (grain boundaries, resulting from aggregation or partial sintering), are key parameters controlling coarsening[22], phase equilibrium[23], and other physical properties [24]. For instance, the stability of $MgAl_2O_4$ as a catalytic support is strongly affected by its surface energy, and the material shows improved resistance to coarsening when the surface energy is lowered by the addition of dopants.[25] This is attributed to a reduction in the driving force for the process, and has been discussed in this context for many different oxide systems.[15] The impact of surface and grain

boundary energy can also be seen in the polymorphism of TiO_2, in which the relative stability of anatase to rutile is impacted by the relative fraction of each interface.[23,26] It was later demonstrated it is also possible to control such transformation by targeting interfacial energies[27–29], which is a concept that could be better explored in the context of design of more stable LMO nanostructures for cathode application.

Experimental studies on the interfacial energies of Li-ion battery cathode materials are very limited, and the available data is mostly restricted to simulation efforts, which require experimental benchmark.[30–32] A calorimetry study on nanostructured $LiCoO_2$ revealed its surface energy to be in the range of 1.12 – 1.23 J/m^2, which is considered low when compared to other isostructural materials.[33] It was claimed that this relatively low energy suppresses undesirable side reactions in batteries, explaining why $LiCoO_2$ finds widespread application as cathode. This further indicates the design of nanostructured cathodes with low interfacial energies may be an effective strategy to improve cathode stability.[34] In fact, negative effects of high surface energies in cathodes have been demonstrated in other compositions, such as Li_3VO_4.[35]

The surface energy of LMO has been studied by a number of simulation techniques. Li-terminated (001) surfaces has been reported as the most stable surface plane[30,31], similarly to the equivalent Mg-terminated surfaces in the isostructural $MgAl_2O_4$.[30,31] Going beyond the assumptions that the stoichiometric composition of crystal volume extends to its surfaces, Kim et al. studied environmental effects on LMO surfaces, noting that (001) and (111) are fairly close in energy and are the most thermodynamically favorable surfaces, with energies in the order of 0.75 J/m^2 for Li-terminated reconstructed surfaces.[32] Warburton et al. further studied surface energies of LMO under a range of Li and O chemical potentials in which bulk LMO is stable, showing Li/O and Li-terminated (111) surfaces are energetically favored.[36]

As a novel strategy to manipulate functional properties of nanomaterials, Hasan et al. demonstrated by atomistic simulations and experiments (calorimetry) that surface energies of $MgAl_2O_4$ can be reduced by using dopants prone to segregation.[25,37] The segregation was in fact a spontaneous formation of surface excess[22] where trivalent dopants substituted Al^{3+} at the surfaces, leading to surface energy decrease due to better satisfied coordination of local ions. While all surface energies were generally reduced, some surface planes were more affected strongly than others, resulting in an increase in the fraction of (111) surface.[37] Similar effects on the thermodynamics of grain boundaries were observed when doping $MgAl_2O_4$ with rare-earth elements.[38] Σ3 (111) grain boundaries were studied by atomistic simulation and indicated the segregation of trivalent rare-earths such as La^{3+}, Y^{3+}, and Gd^{3+}, leading to grain boundary energy reduction, as confirmed by calorimetry.[38]

Recently, the role of grain boundaries in cathode degradation mechanisms have been investigated[39], supporting evidences that nanoscale crack formation at grain boundaries are critical barriers for high voltage applications.[6,8,9,11,12] A relationship between grain boundary energetics and fracture toughness in nanoceramics has been proposed by Bokov et al.[40]. The concept indicates that doping of LMO grain boundaries could be an effective strategy to reduce excess energies and increase fracture toughness. Some studies have shown that doping LMO with small concentrations of metal ions, such as Al^{3+}, Gd^{3+}, Dy^{3+}, or Nd^{3+}, can indeed mitigate capacity fading during extended cycling by inhibiting Jahn-Teller distortion and dissolution of Mn ions.[10,41–43] The dopant effects were attributed to changes in the crystalline structure, including cell dimension, atomic arrangements, and bonding strengths. The effect of 'dopants' on interfacial properties are typically only considered when they are applied as 'surface coatings', which have themselves shown significant improvements in cyclability.[7] However, to

the best of our knowledge, the impact of spontaneous segregation of dopants to LMO interfacial energies has not been addressed in depth.

In this study, the average surface and grain boundary excess energies of fully oxidized spinel LMO nanoparticles, synthesized via flame spray pyrolysis (FSP), were experimentally assessed using calorimetry. The data enabled a comprehensive and quantitative description of the total excess energies in nanocrystalline LMO. In order to investigate the effect of an interfacial segregant, Sc-doped LMO nanoparticles were synthesized and both interfacial energies were quantified. Scandium was observed to significantly lower the surface energy of nanoparticles, increasing the overall stability against thermal coarsening and reducing surface reactivity. We then discussed how this surface energy lowering have potential implications on LMO polymorphic stability during Li^+ deintercalation in Li-ion battery.

Experimental

Synthesis

LMO nanoparticles were synthesized using a custom-built FSP reactor using natural gas as fuel and a mixture of air and oxygen as carrier and oxidizing gas. FSP is a one-step, scalable process which enables production of nanoparticles with a variety of compositions through fast evaporation of the liquid precursor followed by nucleation of oxide particles in a high temperature flame.[44–48] Previous studies report that nanoparticles of battery cathode materials such as LMO, $LiCoO_2$ and $LiFe_5O_8$ with consistent electrochemical properties can be synthesized using FSP.[46] Lithium nitrate ($LiNO_3$, Sigma-Aldrich, >98.0 %) and manganese nitrate hydrate ($Mn(NO_3)_2.xH_2O$, Sigma-Aldrich, >98.0 %) were dissolved in deionized water to produce 0.1 M nitrate solution which was used as precursor to the reaction. For the synthesis of 2

mol% Sc_2O_3-doped LMO, scandium nitrate hydrate ($Sc(NO_3)_3.xH_2O$, Sigma-Aldrich, 99.9%) was added to the precursor solution to obtain the desired molar ratio of Sc to Li and Mn ions. In this reactor, ultrasonic atomizers generated microscopic droplets of the precursor solution which were introduced to a torch by a carrier gas (~16 L/min) and were evaporated and oxidized rapidly in the flame. The fuel flow rate was 1 L/min. The oxidized nanoparticles were deposited in the sample collector placed around the flame. The obtained nanoparticles were further annealed under pure oxygen at 450 °C for 2 hours in a tube furnace (GSL-1700X, MTI Corporation, California, USA) and grinded.

Characterization

Crystallographic phase and crystallite size analyses of the synthesized nanoparticles were carried out using X-ray diffraction (XRD, Bruker AXS Inc. Madison, USA) with Cu Kα radiation (λ = 1.5406 Å) operated at an accelerating voltage of 40 kV and an emission current of 40 mA. Crystallite size was calculated using whole profile fitting in JADE 6.1 (MDI) software. The chemical composition was analyzed using inductively coupled plasma mass spectrometry (ICP-MS) with GLI procedure ME-70 by Galbraith Laboratories, Inc. to quantify Sc, Li and Mn in the samples. Surface area was analyzed by Brunauer-Emmet-Teller (BET) method with nitrogen adsorption using a Gemini VII Surface Area Analyzer (Micromeritics Instrument Corp., Norcross, USA). Grain size and morphology of sintered samples were analyzed using a scanning electron microscope (SEM, FEI 430 Nano-SEM instrument, FEI Company, Hillsboro, Oregon) and the obtained images were analyzed using Image J software. For structural details of the samples, X-ray photoelectron spectroscopy (XPS) was performed using a conventional XPS spectrometer (ScientaOmicron ESCA+) coupled to a high-performance hemispheric analyzer

(EAC2000) with a monochromatic radiation excitation source of Al Kα (hν = 1486.6 eV). The measurements were carried out in an ultra-high vacuum, 10^{-9} Pa, in an appropriate chamber (UHV). The high-resolution XPS spectra were recorded with a constant pass energy of 20 eV with 0.05 eV per step and later analyzed with Origin.

Surface and grain boundary energy measurement

Surface and grain boundary energies of undoped and Sc-doped LMO were measured using the nanoparticles' heats of sintering and microstructure analyses of the samples before and after sintering. This methodology has been validated for various metal oxide systems and is based on the concept that the exothermic heat of sintering is quantitatively related to the change in surface and grain boundary areas and their associated energies.[17,49–53] The energy released during sintering can be expressed with the following equation:

$$\Delta H_{\text{sintering}} = \Delta A^{S} \times \gamma_{S} + \Delta A^{GB} \times \gamma_{GB} \quad (1)$$

where $\Delta H_{\text{sintering}}$ is the heat of sintering, which corresponds to the energy released by the system as a result of thermally induced coarsening, ΔA^{S} and ΔA^{GB} are the change in surface area and grain boundary area during sintering, and γ_{S} and γ_{GB} are surface and grain boundary enthalpies, respectively. In equation (1), γ_{S} and γ_{GB} are unknowns, while the other parameters can be experimentally quantified. $\Delta H_{\text{sintering}}$ was measured using a differential scanning calorimeter (DSC) and ΔA^{S} was measured by nitrogen adsorption (BET). ΔA^{GB} was calculated by deriving the total interfacial area of all particles using grain size and morphology data, subtracting the BET area (i.e. surface area) from this value, and dividing by two (because two surfaces create one grain boundary during sintering).[54] The actual shape of the particles analyzed by microscopy was considered in the calculations as it affects the area to volume ratio.[54] Based

on this concept, a set of at least two DSC sintering experiments and microstructure analyses allowed solving Eqn. (1) for surface and grain boundary energies.

Noteworthy, during sintering itself, changes in *entropy* are added driving force of the process, affecting coarsening behavior. However, the experiment for measuring interfacial energies is performed within a DSC. Calorimeters only measure the enthalpic effects of reactions by thermodynamic principle. Therefore, the measured heat released can be directly related to interfacial enthalpies. In this work, we further assume interfacial 'enthalpies' and 'energies' to be the same because of the negligible effect of entropy to the total thermodynamics. Entropic effects on oxide nanoparticles have been studied by a number of researchers, and the most prominent ones suggest most entropic effects comes from chemisorbed water, rather than the surface chemistry itself.[55] During sintering, the amount of water is negligible. Nevertheless, the surface entropy in oxide surfaces should be rather small, <1.5 $J \cdot K^{-1} \cdot mol^{-1}$ [56], meaning that at temperatures below 800°C, its contribution is deemed negligible and interfacial energies and enthalpies can be safely considered the same [57].

For $\Delta H_{\text{sintering}}$ measurements, the synthesized nanoparticles were pressed into 5 mm diameter pellets using a hydraulic press at 100 MPa. The pellets were then sintered inside of a DSC (DSC 404 F1 Pegasus, Netzsch Instruments, Selb, Germany, calibrated with heat capacity of sapphire single crystal) which recorded the heat effects during the process. Sintering temperatures for the DSC tests were determined using thermogravimetry (TG) in a SETSYS Evolution TGA/DSC, Setaram, Inc., Caluire, France. This was done in order to ensure the heat effect due to sintering does not overlap with other possible energetic processes, such as reduction/oxidation of Mn, evaporation of Li, or water desorption – which is of prime importance for the validity of Eqn. (1). For the sintering experiments using DSC, the instrument

was set to heat up to the target temperature at 20 K/min, followed by a 10 min isotherm and controlled cooling. The same cycle was repeated three times without removing the sample. To calculate $\Delta H_{\text{sintering}}$, the DSC signal from the third run was used as baseline and was subtracted from the signal from the first cycle. We used the third run as baseline because at that point no heat effect related to sintering was observed, i.e. as particles were already coarsened and only heat capacity is observed during the subsequent DSC heating cycle. Exothermic DSC peaks were then integrated and corresponded to $\Delta H_{\text{sintering}}$.

For interfacial energy measurement of undoped LMO, samples with varying initial crystallite sizes were prepared by calcining the as-synthesized LMO nanoparticles at 625 °C, 650 °C and 675 °C for 1 hour, respectively. Three sets of DSC sintering experiments were also performed for Sc-doped LMO, but using a fixed initial crystallite size, achieved by calcining nanoparticles at 625 °C for 1 hour, and varying the maximum DSC sintering temperature (770 °C, 775 °C and 780 °C) to allow for distinct interfacial evolution and solvability of Equation (1).

Dopant distribution in Sc-doped LMO nanoparticles

Spatial distribution of Sc in doped LMO nanoparticles were analyzed using scanning transmission electron microscopy coupled with electron energy loss spectroscopy (STEM-EELS) using JEOL 2100F (S)TEM. The TEM was operated with accelerating voltage of 200 kV and the EELS spectrum images were acquired with a Gatan Tridiem post-column Spectrometer. The obtained EELS data was processed with digital micrograph 3.0 using a power-law function to remove the background, and the integration window widths used for creating the spectrum images were 25 eV for O and Mn and 10 eV for Sc.

Surface reactivity and stability against coarsening evaluation

In order to evaluate the correlation between surface energy and surface reactivity of the synthesized nanoparticles, water adsorption calorimetry was carried out on as-synthesized undoped and Sc-doped LMO. Water adsorption calorimetry technique involves an experimental setup consisting of a water vapor dosing system (3Flex, Micromeritics Instrument Corp.) attached to a DSC (Sensys Evo, Setaram Inc.). The 3Flex is used to (1) dry samples under vacuum and heat to achieve an anhydrous surface state and (2) to dose controlled amounts of water vapor (in μmoles) to gradually cover the surface. The system records the quantity of adsorbed water on the sample as a function of relative pressure, while the DSC records the heat released at every water dosage. From a thermodynamic point of view, the measured heat represents the energy of water adsorption to the surface of the sample. This is a quantitative measure of the extent at which the anhydrous surfaces can be stabilized by water adsorption.[33,58–60] Larger heats of adsorption indicate higher reactivity and, therefore, higher surface energies. Recently, this technique combined with a theoretical model has been used to directly quantify the absolute surface energy of nanomaterials, but this is not being performed here.[60–62]

Stability of undoped and Sc-doped LMO samples against coarsening at elevated temperatures was also studied to evaluate the effect of Sc-doping. The as-synthesized undoped and Sc-doped LMO nanoparticles were coarsened by heating up to 450 °C, 550 °C, 650 °C and 750 °C for 1 hour in a tube furnace (GSL-1700X, MTI Corporation, California, USA) and the crystallite sizes and specific surface areas of the resulting samples were analyzed using XRD, BET and SEM, as described in this characterization section.

Results and Discussion

Synthesis and nanoparticle characterization

Figure 1 shows the XRD patterns of the as-synthesized LMO powders, with respective crystallite sizes and stoichiometry listed in Table 1. The data confirms FSP produces nanoparticles with grain sizes around 20 nm, slightly rich in Li, possessing the characteristic spinel structure and with no detectable second phases or impurities. The XRD pattern for Sc-doped LMO (Figure 1) shows a similar spinel structure, revealing that the small concentration of Sc did not change the crystallographic phase, while the ICP result (Table 1) confirmed the presence of Sc at 3.4 mol%.

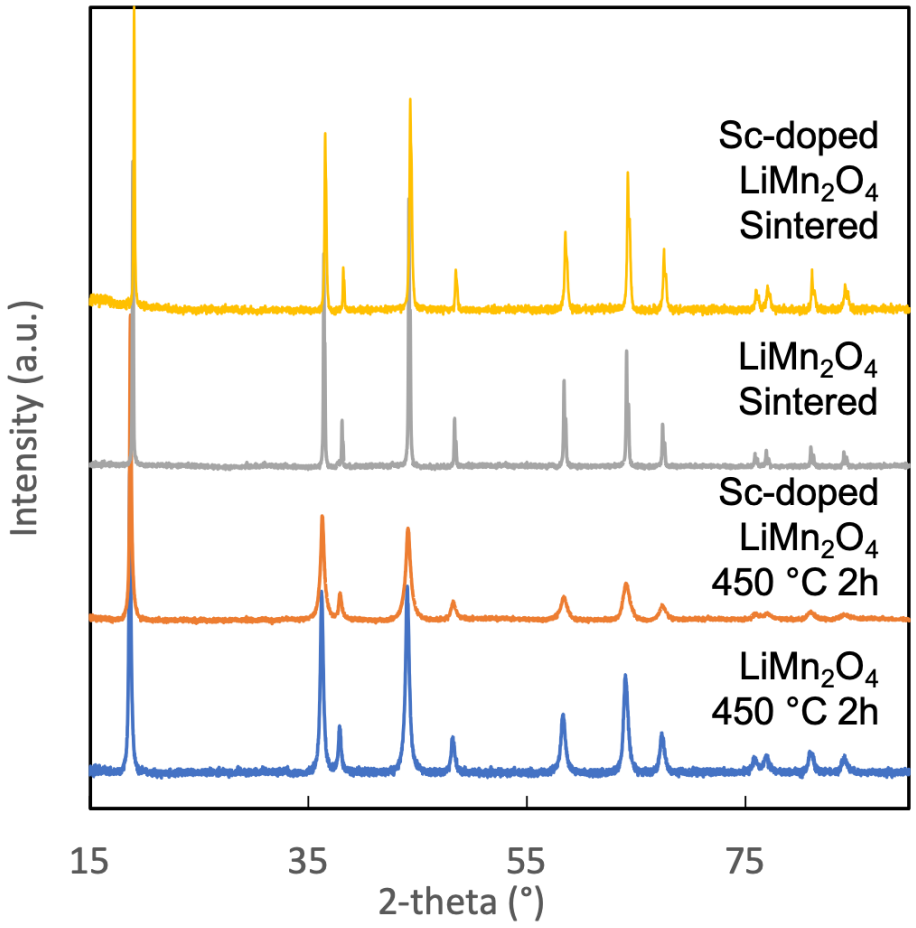

Figure 1. XRD patterns of undoped and Sc-doped LMO calcined at 450 °C for 2 hours and after sintering.

Table 1. Crystallite size and stoichiometry of the undoped and Sc-doped LMO.

	Crystallite size (nm)	Stoichiometry		
		Sc	Li	Mn
Undoped LMO 450 °C 2 h	20.8 ± 1.0	-	1	1.88
Sc-doped LMO 450 °C 2 h	19.8 ± 1.0	0.034	1	1.83

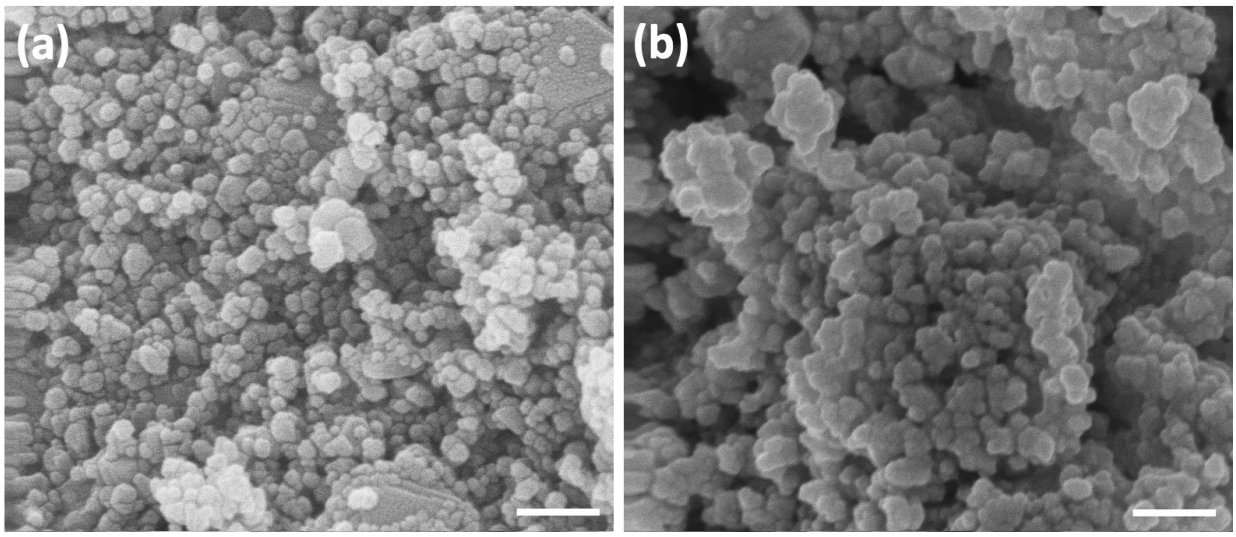

Figure 2. SEM images of undoped and Sc-doped LMO calcined at 625 °C for 1 hour. The scale bars indicate 200 nm.

Figure 2 shows SEM images of undoped and Sc-doped LMO calcined at 625 °C for 1 hour. The images show isotropic grains with dimensions consistent with the crystallite size obtained by XRD (Figure S1, Table 2). Fairly homogeneous size distribution is observed, with some clear agglomerations. Such agglomeration is often observed in samples synthesized using FSP and is related to the formation of microscale secondary particles consisting of the nanoscale primary

ones.[44–46] The size of such secondary particles reflects the dimensions of the liquid precursor droplets introduced to the flame (atomized aqueous solution).[63]

Surface and grain boundary energy measurement of undoped and Sc-doped LMO

The method to measure surface and grain boundary energies relies on the quantitative recording of the heat flow resulting from the microstructural evolution occurring during thermally activated sintering. As detailed in the experimental section, it is necessary to avoid any parallel reactions other than coarsening itself during the test, so that the heat effect can be reliability attributed to the interfacial area evolution alone (see equation 1). TG/DSC results (Figure S2) indicated a high temperature limit is required for this condition to be met. The temperature for sintering of undoped LMO in the DSC cannot not exceed 800 °C, which is the temperature at which a mass loss associated with Mn reduction is observed in the TG/DSC.[64,65] No other parallel reactions were observed below 800 °C.

Figure 3(a) shows the DSC peaks for three representative undoped-LMO specimen with different initial crystallite sizes (Table 2). The exothermic effects were observed for all samples to start at temperatures above their calcination temperatures. The integrated data shows $\Delta H_{\text{sintering}}$ decreases with the increase in the temperature of calcination prior to sintering. This is a consequence of the different initial crystallite sizes (Table 2) and results from the fact that larger grains present lower driving force for sintering due to their reduced interfacial areas (A_S^I and A_{GB}^I). Confirming that the measured heat effect could be attributed to sintering alone, ICP and XRD analyses on samples after DSC sintering showed no change in Li to Mn ratio or crystal structure (Figure 1), indicating that there was no loss of Li or phase transitions during the DSC experiments. Additionally, the surface chemical composition of LMO nanoparticles before and

after DSC was investigated by XPS and are summarized in Figure 4 and Figure S3. Li 1s core level spectrum was observed for both samples (before and after sintering) centered at 53.0 ± 0.2 eV and attributed to Li^+ in LMO.[66,67] This corroborates with the ICP results showing that the ratio of Li to Mn is not affected by the heating profile in DSC run. Mn3p spectra (Figure 4) was also detected and evaluated in terms of Mn oxidation states. The doublets energies present in the Mn 3p orbital centered at ~50 and 48 eV are signatures for the Mn^{4+} and Mn^{3+} states, respectively. Figure 4(a) shows that before and after DSC sintering of the undoped samples, both Mn^{3+} and Mn^{4+} are present, which is in agreement with the literature[66–69] but with a particularly higher concentration of Mn^{4+} (a feature claimed by Reddy et al. to have a possible relation to improved cycling performance[69]). No significant differences in terms of Mn^{3+} to Mn^{4+} ratio was observed when comparing samples before and after sintering, which indicates the absence of oxidation state changes during the test [70].

Figure 3(b) shows DSC peaks obtained from sintering Sc-doped LMO up to 770 °C, 775 °C and 780 °C. Equivalent characteristic exothermic heat effects associated with sintering were observed here. Consistently with the undoped LMO, no parallel reactions, such as phase transitions and Mn reduction, were observed during the sintering experiments, as shown by the collective data in Figure 1, Figure 4 and Figure S3. XPS data performed on the Sc-doped samples (Figure 4(b)) showed a mixed valence of Mn^{3+} and Mn^{4+}, which, consistently with undoped samples, showed a higher population of Mn^{4+} state and remained unchanged before and after sintering. A slightly higher ratio of Mn^{3+} states on Gauss-Lorentz deconvolution for Sc-doped when compared to undoped samples was observed and is likely related to the presence of Sc changing the Mn surrounding environment.

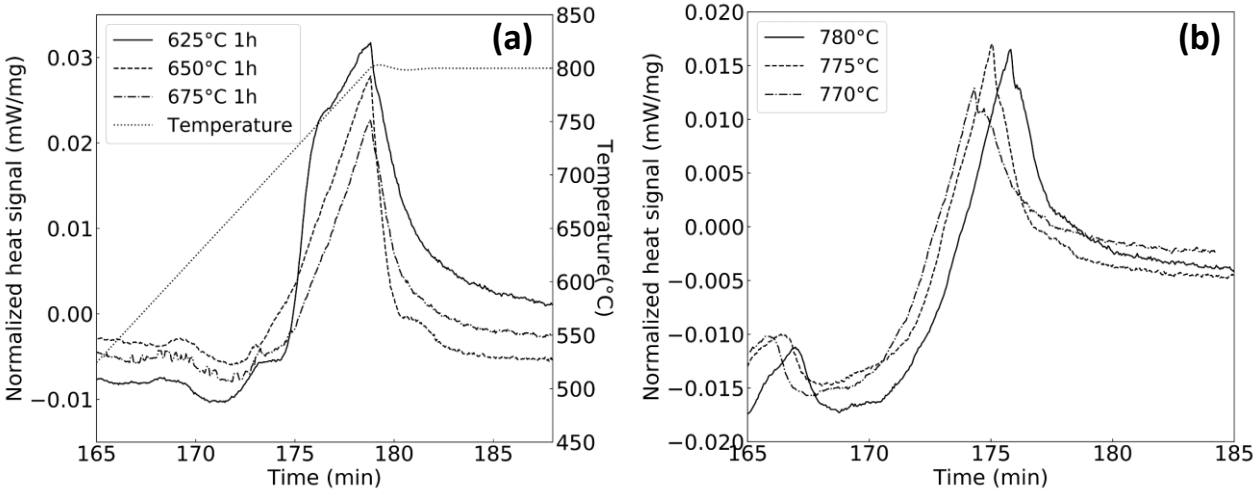

Figure 3. Exothermic DSC peaks of sintering of (a) undoped and (b) Sc-doped LMO.

Table 2. Initial crystallite size (D), initial surface and grain boundary area (A_S^I and A_{GB}^I), final surface and grain boundary area (A_S^F and A_{GB}^F), and $\Delta H_{sintering}$ of samples used for surface and grain boundary energy measurements of undoped and Sc-doped LMO.

Sample	Calcination/ Sintering temperature	D (nm)	A_S^I (m^2/g)	A_{GB}^I (m^2/g)	A_S^F (m^2/g)	A_{GB}^F (m^2/g)	$\Delta H_{sintering}$ (J/g)	γ_s (J/m^2)	γ_{GB} (J/m^2)
Undoped	625 °C 1h/ 800°C	42.1 ± 2.1	17.7 ± 0.1	5.2 ± 1.4	4.0 ± 0.1	1.2 ± 0.2	12.8 ± 0.4	0.85 ± 0.04	0.27 ± 0.07
Undoped	650 °C 1h/ 800°C	48.0 ± 2.0	12.5 ± 0.1	7.6 ± 1.2	5.9 ± 0.1	1.7 ± 0.3	7.4 ± 0.4		
Undoped	675 °C 1h/ 800°C	53.4 ± 2.2	12.9 ± 0.1	7.0 ± 1.1	6.5 ± 0.1	0.5 ± 0.2	7.0 ± 0.8		
Sc-doped	625 °C 1h/ 770 °C	34.8 ± 1.9	9.9 ± 0.1	18.9 ± 2.7	4.0 ± 0.1	9.3 ± 0.5	5.3 ± 0.5	0.48 ± 0.17	0.24 ± 0.02
Sc-doped	625 °C 1h/ 775 °C				3.9 ± 0.1	5.6 ± 0.2	5.7 ± 0.4		
Sc-doped	625 °C 1h/ 780 °C				3.9 ± 0.1	4.6 ± 0.3	6.6 ± 0.6		

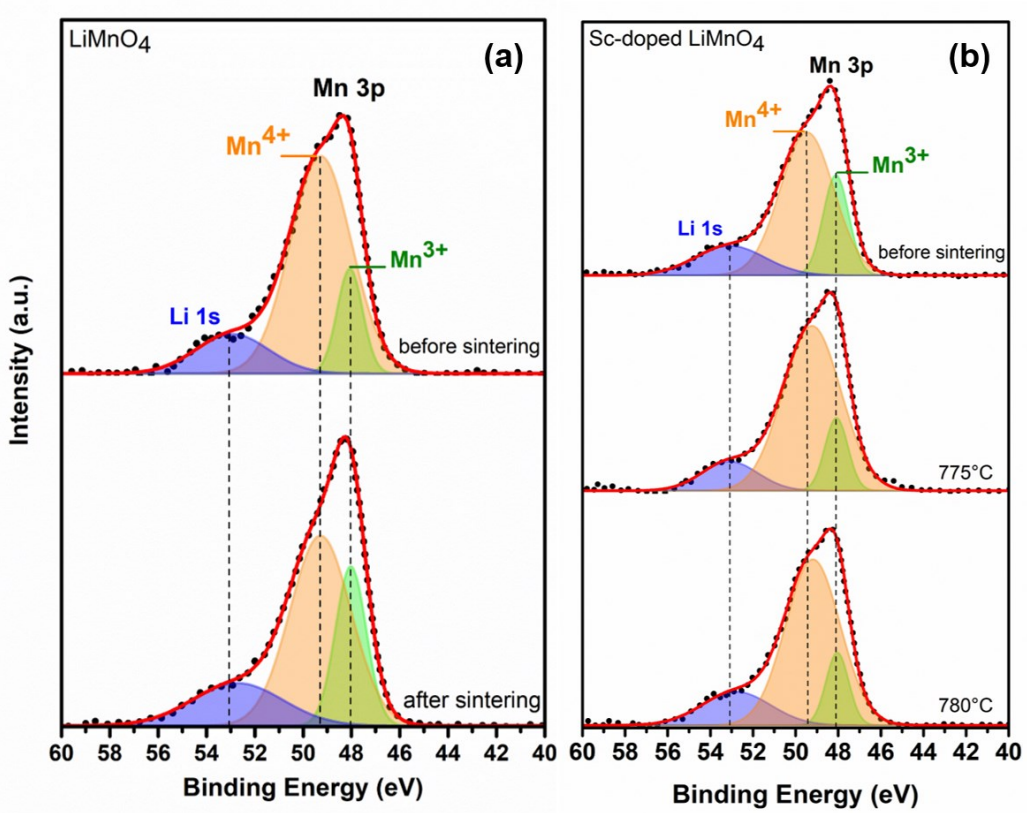

Figure 4. Mn3p core level XPS for (a) undoped and (b) Sc-doped LMO samples before and after sintering.

Figure 5 shows the SEM images of the undoped and Sc-doped samples after the DSC experiments. While there is not much difference in the grain sizes and morphologies between undoped and doped samples, there is an obvious heterogeneity in the grains with two distinct morphologies and apparently bimodal size distribution. This is likely due to the agglomeration of nanoparticles prior to sintering as was observed in Figure 2. While grain sizes are known to be correlated with sintering rate following Herring scale law, high packing density within agglomerates often leads to faster local sintering, introducing larger particles in the sintered product.[71] Although the bimodal grain sizes in Figure 5 resemble characteristics of abnormal grain growth, which is typically caused by variations in grain boundary characteristics, such as

roughness, anisotropy in grain boundary energies, and presence of impurities, [17,72] this is less likely in the present case as the grains before sintering showed isotropic morphology with no signs of chemical impurities.

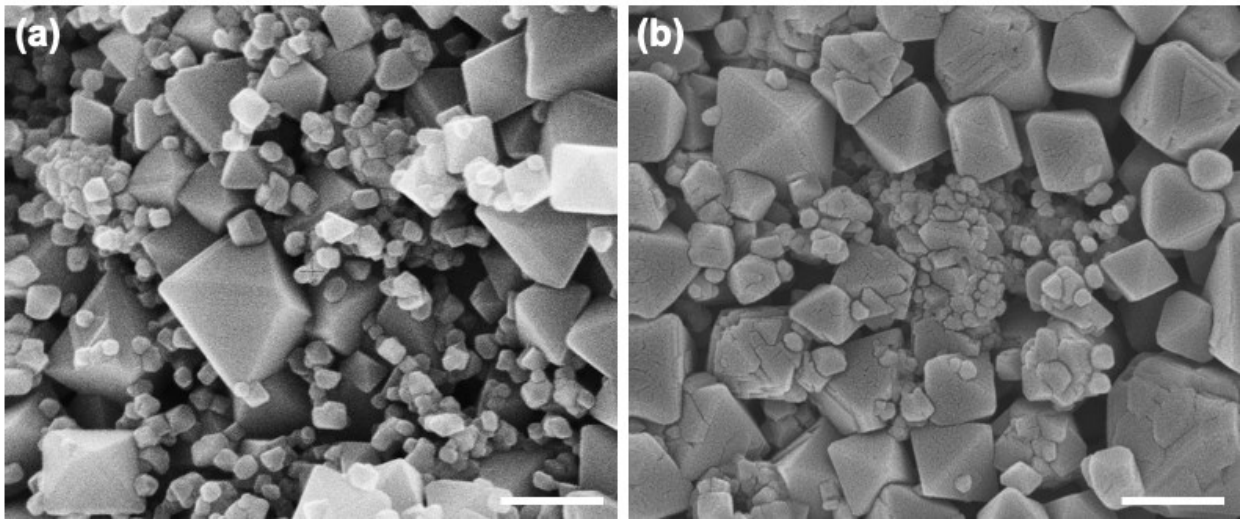

Figure 5. SEM images of samples after DSC sintering. (a) undoped LMO sintered up to 800 °C and (b) Sc-doped LMO sintered up to 780 °C. The scale bars represent 500 nm.

In order to enable proper determination of interfacial areas for calculation of the respective energies from the integrated heat of sintering (equation 1), the heterogeneity in morphology was mathematically considered using shape factors representing different grain morphologies. Based on the SEM images (Figure 5), the larger grains were approximated as octahedrons and smaller grains as tetrakaidekahedrons. The octahedral grains are commonly observed in LMO and the morphology has been identified as one of the equilibrium shapes of LMO consisting of 8 (111) planes of the spinel structure.[31,36,73] The shape factor was calculated from the surface area to volume ratio of each morphology and was 8638 for octahedrons and 7100 for tetrakaidecahedrons, respectively.[54] In addition to the shape factors, volume fractions of each type of grains were quantified from the SEM images to calculate the total interfacial area in the

samples after DSC sintering. This was done by converting the areal fraction of each grain from at least 10 SEM images per sample to volume fraction, which was possible due to the isotropic morphologies of the grains.

Using the obtained data, surface and grain boundary energies of undoped LMO were calculated to be 0.85 ± 0.04 J/m^2 and 0.27 ± 0.07 J/m^2; and of Sc-doped LMO to be 0.48 ± 0.17 J/m^2 and 0.24 ± 0.02 J/m^2, respectively. While surface and grain boundary energies can depend on temperature and properties of interfaces such as crystallographic planes, atomic configurations and stoichiometry, the used method provides average values representing existing orientations of interfaces and the temperature range used in the DSC experiments. While there is limited to no experimental data on surface and grain boundary energies of LMO in the literature, the present results were compared to some computational studies on LMO surface energy data.[30–32,36,42] For example, Kim et al. derived (001) and (111) surface energies using density functional theory (DFT) as 0.72-0.82 J/m^2 and 0.77-0.84 J/m^2, respectively, which varied depending on different approaches used to define surface structures.[32] Benedek et al. and Karim et al. also reported similar values for (111) surfaces which are in good agreement with the present experiment value.[30,31] While the distribution of different surface orientations in the samples is not known in our work, the surface energy result may indicate that (001) and (111) surfaces are the dominant ones, as demonstrated by the observed octahedral morphology after sintering (Figure 5).[74,75] When compared to the experimental surface energy of another cathode material, the present surface energy of LMO is lower than that of $LiCoO_2$ (1.12 J/m^2) measured using a combination of water adsorption and drop solution calorimetry.[33] This lower surface energy of LMO may support the advantages of LMO over $LiCoO_2$ especially in nanostructured cathode, indicating its higher thermodynamic stability.

Both surface and grain boundary energies in LMO are also lower as compared to other isostructural spinel materials. The values are almost half of spinel $MgAl_2O_4$ and $ZnAl_2O_4$ interfacial energies reported using similar methodologies, indicating high stability of LMO interfaces.[76,77] It is tempting to speculate that this is related to the localized presence of excess Li^+ at both interfaces, as suggested by computational studies on surface reconstruction in LMO and other Li^+ containing materials.[31,36] Calculations of LMO surface energies at various orientations have shown that Li-terminated surfaces are indeed thermodynamically more favorable than those terminated with other species (O^{2-} and Mn ions).[30,31,36,42,78] Moreover, DFT calculations showed that Li^+ diffusion can play a major role in reconstruction, thus enabling stabilization of LMO (111) surfaces through a mechanism with very low kinetic barrier even at ambient condition.[36] Similar results have suggested that low charge cations localized on interfaces can lead to more stable surfaces in other materials, including $LiFePO_4$ and $LiCoO_2$. For instance, the surfaces with Fe ions were reported to be more reactive (higher energy) than those with Li^+ in $LiFePO_4$; similarly, Co ions localized at interfaces with lower coordination number as compared to bulk Co in $LiCoO_2$ were shown to be more energetic than Li^+ accommodating similar lower coordination.[78,79] This suggests that the presence of Li^+ in LMO, rather than the cations with valence of 2+ or 3+ in $MgAl_2O_4$ and $ZnAl_2O_4$, may contribute to the stabilization of interfaces, leading to their lower energies. The effect of Li^+ in lowering surface energy of LMO is also reflected in the much higher surface energy of Mn_3O_4 (1.62 J/m^2) despite being isostructural to LMO.[80] The same mechanism might be responsible for the low grain boundary energy of LMO. As suggested by Li^+ diffusion studies in LMO, the diffusion coefficient of Li^+ at the grain boundaries is significantly higher than in the bulk, indicating high mobility of Li^+ to better accommodate high energy grain boundary defects.[81]

The effect of Sc in lowering the surface energy of LMO is evident from the data in Table 2, showing a decrease of about 50 %. Meanwhile, the grain boundary energy remained almost unchanged. Similar effects have been observed in other spinel systems, such as $MgAl_2O_4$, where the trivalent dopants lowered its surface and grain boundary energies by interface segregation directly detected using STEM-EELS.[25,37] Figure 6 shows the STEM-EELS data obtained from Sc-doped LMO nanoparticles visualizing the spatial distribution of Sc. The image shows a grain and an associated grain boundary. The color maps for O and Mn show that these elements are distributed throughout the bulk of the grains homogeneously. The concentrations of O and Mn appear lower near the surface and the grain boundary as the electron beam interacts with less volume of the grains in those regions. On the other hand, the color map for Sc shows its localized concentration at the grain boundary as well as a small enrichment at a portion of the surface and throughout the bulk of the grains. This suggests that Sc preferentially segregates to grain boundaries despite the dopant's negligible effect on grain boundary energy, and that the direct cause of surface energy lowering is likely not only dopant segregation to surfaces.

Higher degree of dopant segregation at grain boundaries as compared to surfaces has been observed in other doped nanoparticles, such as CeO_2 doped with transition metals and Mn-doped yttria-stabilized zirconia (YSZ).[21,82] According to the theories of stability of nanomaterials, ionic dopants can either segregate to interfaces, form solid solution with the host, or precipitate as second phases depending on the thermodynamic favorability of each phenomenon.[28,29,83] The present results reflect the low solubility of Sc into LMO, the absence of second phase precipitation, and higher affinity of the dopant to grain boundaries over surfaces. The possible explanation for the limited effect of Sc on the grain boundary energy of LMO is that Sc is replacing Li^+ at the grain boundaries. As discussed before, Li^+ excess at interfaces is likely

responsible for energy lowering in undoped LMO, and therefore, the exchange of Li^+ by a dopant that can also lower the grain boundary energy may have limited the overall energetic impact of Sc-doping. We admit that this is speculative and hope that further computational studies on the ion distributions in LMO may support this theory.

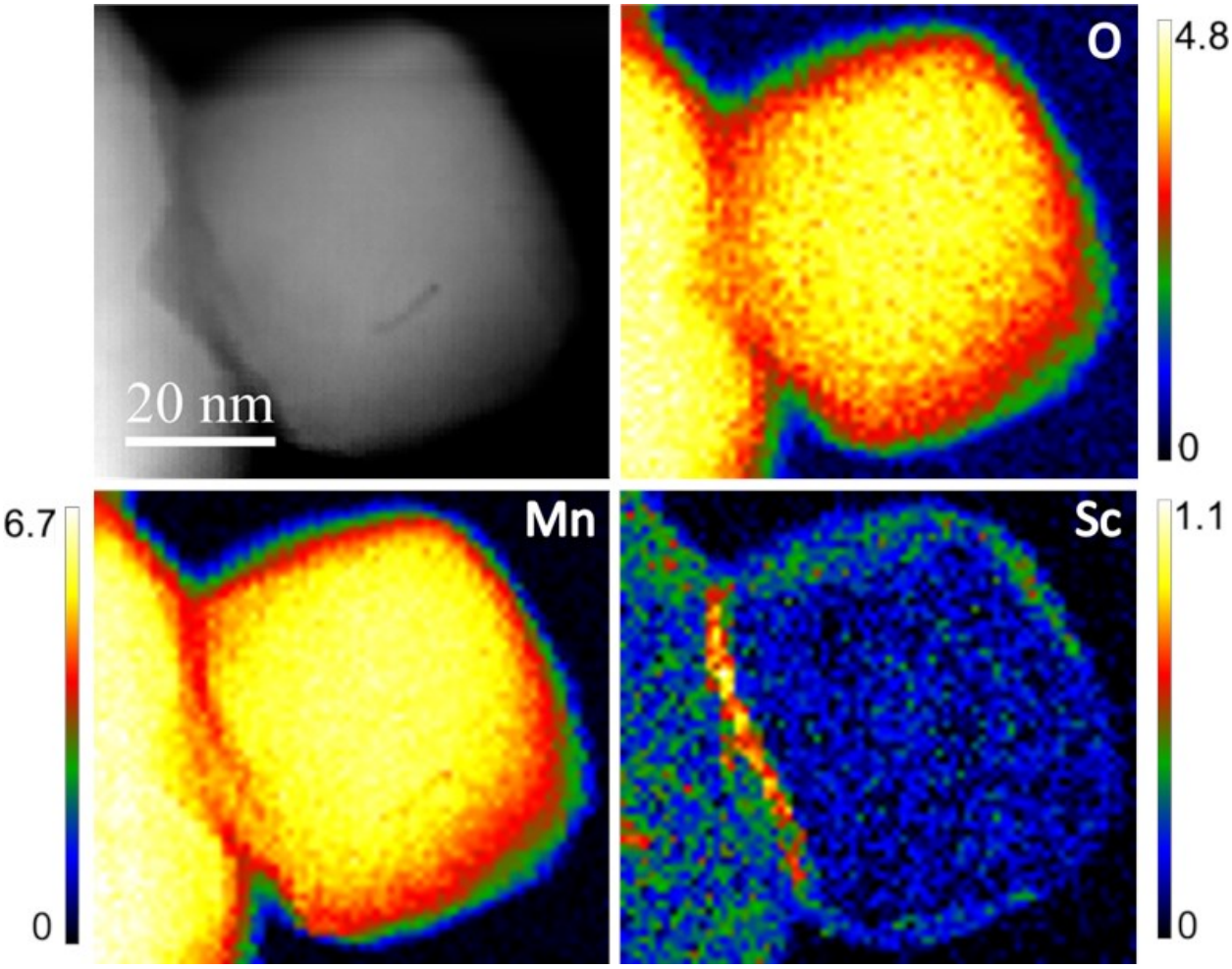

Figure 6. STEM image of the Sc-doped LMO nanoparticles and color maps representing the concentrations of elements O, Mn and Sc around a grain and its grain boundary, as indicated in the figure.

Evaluation of interface stability – water adsorption calorimetry and coarsening study

The stability of the interfaces in undoped and Sc-doped LMO nanoparticles were evaluated by using water adsorption calorimetry and coarsening experiments. Water adsorption calorimetry can be used to directly quantify the surface reactivity of nanoparticles by introducing water molecules to anhydrous surfaces and measuring the heat evolution during the process.[60,61] Figure 7 shows water adsorption isotherms for undoped and Sc-doped LMO nanoparticles (a) and differential enthalpy of water adsorption (kJ per 1 mol of adsorbed H_2O) as a function of water coverage (number of H_2O per nm^2 of sample surface area) (b). Each data point represents a water dosing event where 2 μmol of water was introduced to the samples starting from anhydrous state with zero water coverage. The anhydrous surfaces (zero water content) were achieved after degassing the samples at 250 °C for 12 hours followed by exposing them to high purity oxygen while cooling down to room temperature. Such treatment led to ~1.5 % mass loss, which is equivalent to the maximum mass loss observed at higher temperature in thermogravimetry and confirms the anhydrous condition. The oxygen was used to oxidize any Mn ions that may have been reduced during the degassing process.[65] The adsorption isotherms have similar shapes for both undoped and Sc-doped samples, both presenting type II isotherm. This is typically obtained for monolayer adsorption followed by multilayer adsorption on non-porous surfaces. The enthalpy of water adsorption was most exothermic at the first water dosages, reflecting the highest reactivity of anhydrous surfaces, and became less exothermic as the water coverage increased.[33,59–61,84] Figure 7(b) shows that the first enthalpy of water adsorption of undoped LMO was -75.2 ± 0.5 kJ/mol and that of Sc-doped LMO was ~13 % smaller at -65.8 ± 0.5 kJ/mol. The enthalpies of water adsorption of Sc-doped LMO following the first dosage were consistently lower than those of undoped LMO, indicating lower reactivity. Smaller enthalpy of adsorption has been previously observed in samples with lower surface energies, which is an obvious

correlation from a thermodynamic perspective.[13,33,37] These water adsorption calorimetry results show that the lower surface energy of LMO indeed led to decreased surface reactivity with water, suggesting that the dopant would be effective in increasing the cathode stability and suppressing reactions that adversely affect the battery performance, including dissolution. This remains to be tested.

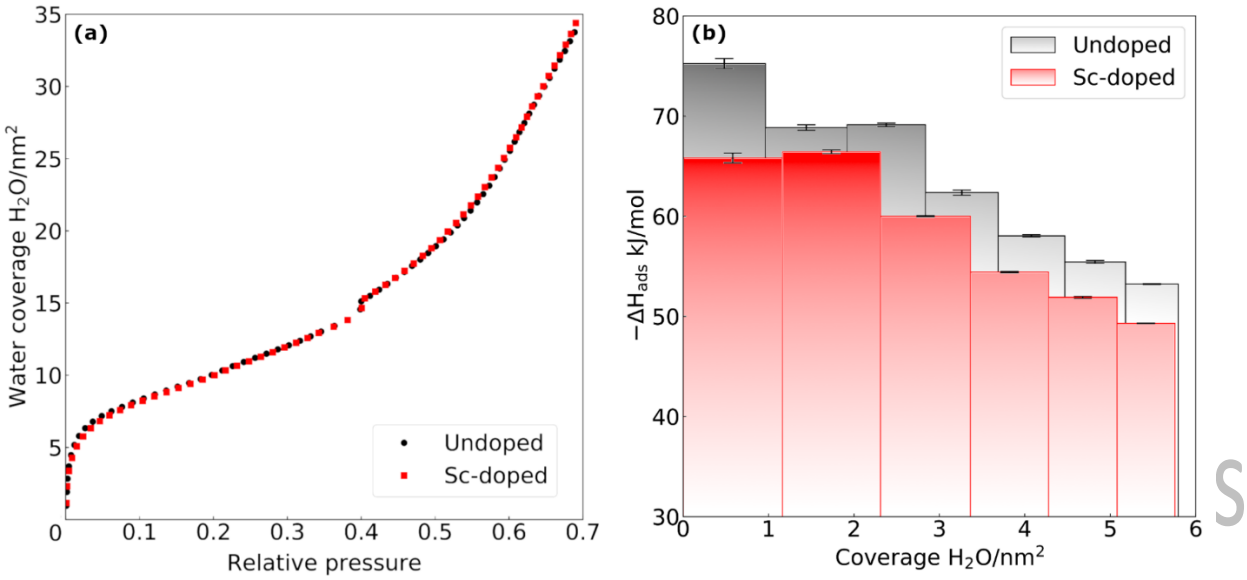

Figure 7. Water adsorption calorimetry results on undoped and Sc-doped LMO as-synthesized nanoparticles. (a) Adsorption isotherm and (b) enthalpy of water adsorption.

While interfacial energies serve as indicators for interface reactivity, in the context of coarsening they act as driving force.[15,17,71] In fact, cycling induced coarsening of cathodes is known as a common degradation mechanism in Li-ion batteries, as it increases resistance at cathode surfaces with decrease in surface potential, while reducing the available surface area for ion exchange with the electrolyte.[85] The phenomenon is a result of the system's lowering the total energy by minimizing surface and grain boundary areas. Therefore, the effect of Sc as an LMO stabilizing dopant was evaluated through a coarsening study, analyzing the microstructure

evolution of undoped and Sc-doped samples when calcined up to 450 °C, 550 °C, 650 °C and 750 °C for 1 hour. Figure 8 shows the evolution of crystallite size calculated from XRD (Figure S4) and BET surface area as a function of temperature. For all studied temperatures, the crystallite sizes for Sc-doped samples were smaller, which is reflected in their consistently larger BET surface areas. The calculated crystallite sizes from XRD were consistent with the SEM observations (Figure S5). This indicates that the lowered surface and grain boundary energies in Sc-doped LMO nanoparticles indeed limited the driving force for sintering and the nanoparticles gained increased stability against coarsening at elevated temperatures, an effect previously observed in other doped nanoparticles.[25,37,86] Moreover, the microstructure (crystallite size and surface area) difference between the undoped and Sc-doped systems remained mostly constant through all temperature range rendering parallel sets of curves. This proportionality (i.e. the growth mechanism remains the same) suggests that the microstructure evolution process is more dominantly controlled by thermodynamics than the kinetics as represented in various grain growth models, highlighting the effect of the lowered interfacial energies.[17]

In addition to lowered surface reactivity and increased stability against coarsening, previous studies suggest that the lowered interfacial energies may introduce other benefits to the functional properties of LMO nanoparticles. For example, mechanical failure, such as intergranular cracking, of cathodes is known to be one of the causes of capacity fading in Li-ion batteries.[6,8,9,11,12] Recently, Bokov et al. showed that doping YSZ nanoparticles with La^{3+} lowers their surface and grain boundary energies, influencing the material's crack propagation behavior in ways that increased its toughness.[40] Crack propagation, from a thermodynamic perspective, is determined by the energy required to produce two surfaces from one grain boundary, and therefore, was strongly influenced by the engineered interfacial energies.[40]

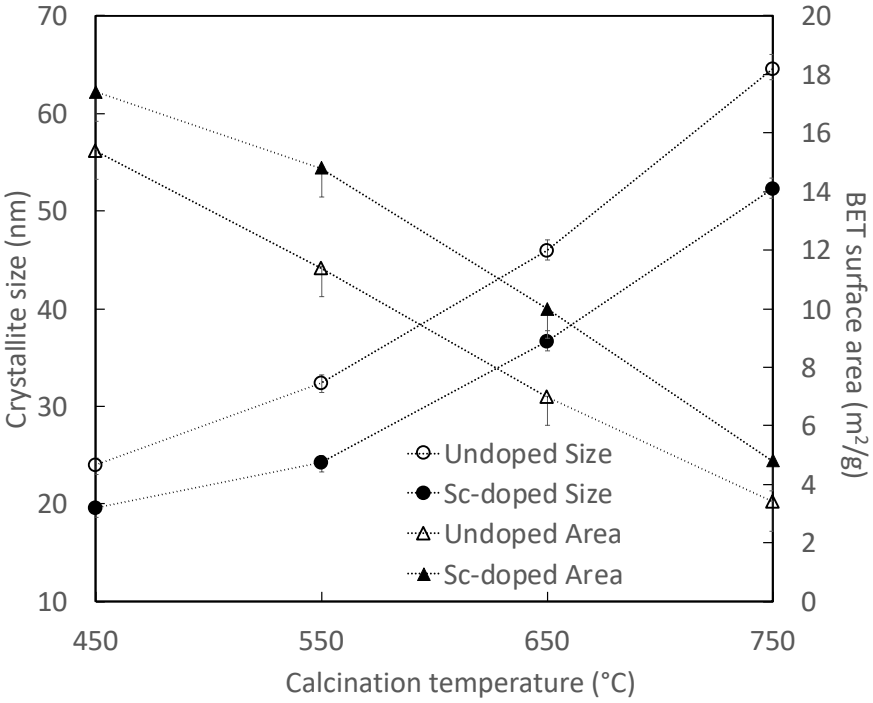

Figure 8. BET surface areas and crystallite sizes of undoped and Sc-doped LMO calcined at varying temperatures.

The effect of Sc-doping on LMO stabilization can also be highlighted by a phase diagram plotting enthalpies of formation and how they are influenced by its surface energy in nanomaterials. Navrotsky et al. has shown that surface energy of materials can play a significant role in thermodynamic stability of various transition metal oxide phases in the form of nanoparticles, creating separate phase diagrams for bulk and nanoscale systems.[13] Figure 9 is a phase diagram plotting the enthalpy of formation of LMO and isostructural spinel Mn_3O_4 as a function of surface area, where the energy at zero surface area is the bulk enthalpy of formation found in literature which increases with the slope equivalent to surface energy of the respective phase.[65,87,88] Comparing the stability of LMO to Mn_3O_4 can be relevant as it represents the phase

transition occurring on the surface of LMO in Li-ion batteries, particularly when takes place.[7,89] While the thermodynamic stability of λ-MnO_2, a manganese phase oxide formed by full delithiation of LMO, could be more relevant in understanding the cathode stability during cycling (varying Li content), its surface energy value was not available for the construction of nanoscale phase diagram.[90]

The phase diagram (Figure 9) shows that even though the thermodynamic stability of bulk LMO and Mn_3O_4 are comparable, after the crossover at 4000 m^2/mol (roughly translates to grain size of ~14 nm) LMO becomes increasingly more stable because of its lower surface energy. This effect is even more prominent in the case of Sc-doped LMO, shifting the crossover at which LMO becomes more stable than Mn_3O_4 to smaller surface area by about 1500 m^2/mol (around ~28 nm). This means that the introduction of the dopant enabled a wider surface area and grain size range of LMO to be stabilized over Mn_3O_4. Recently, Idemoto et al. showed that cathode materials with higher thermodynamic stabilities represented by more exothermic formation enthalpies exhibited improved cycling performance, directly correlating the thermodynamic properties of cathodes with their stability as a battery component.[91,92] They have also shown that the formation enthalpies of LMO become less exothermic, indicating their increased instability, with increasing degree of delithiation (i.e. increasing x in $Li_{1-x}Mn_2O_4$), suggesting that lowering the surface energy of delithiated LMO may be an effective strategy in further stabilizing the cathode during charge/discharge reactions in batteries.[93]

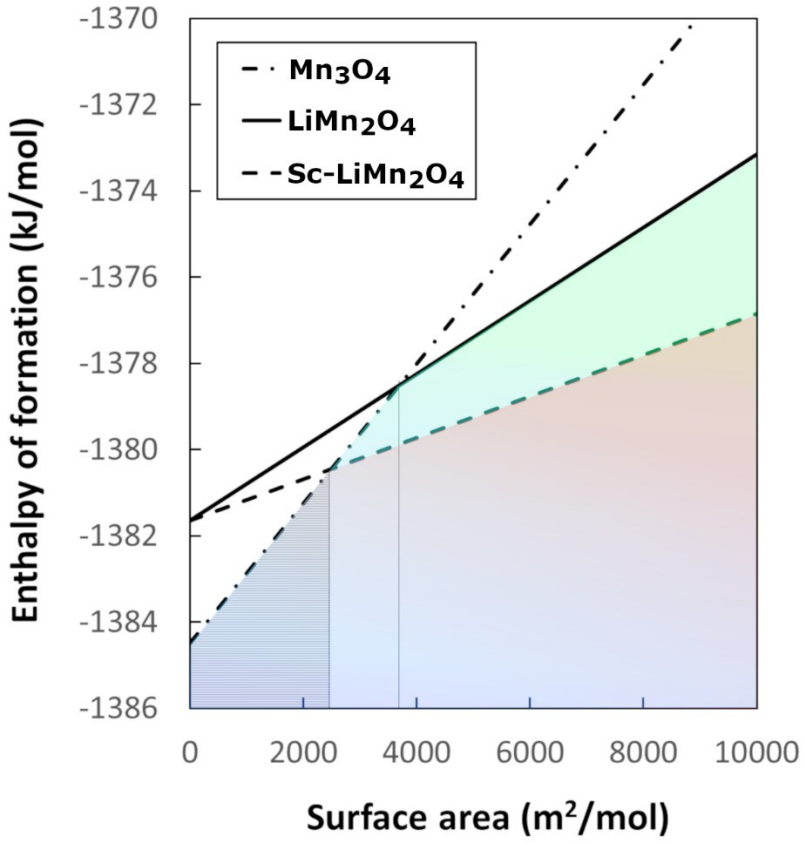

Figure 9. Enthalpy of formation of spinel LMO and Mn_3O_4 as a function of surface area. Sc-doped LMO was assumed to have the same bulk enthalpy of formation as undoped LMO.

Conclusion

Surface and grain boundary energies of nanostructured LMO were experimentally quantified by analyzing the heat effects and microstructure evolution during sintering. Sc-doped LMO showed surface energy significantly lower than undoped LMO likely due to the dopant's segregation to grain boundaries affecting the distribution of Li^+ across the material. The effect of the dopant in stabilizing the surfaces of nano-LMO was evaluated using water adsorption calorimetry and coarsening studies which showed that the surfaces of Sc-doped LMO were indeed less reactive and more stable against coarsening at elevated temperatures than undoped

LMO. The study suggests that this strategy of interface engineering using dopants may be an effective novel approach for improving the stability of Li-ion battery cathode, and therefore, generating batteries with improved capacity retention. This remains to be tested with proper electrochemical tests which are beyond the scope of this work.

Acknowledgements

This work was funded by National Science Foundation DMR Ceramics 2015650.

Supporting Information

Supplemental figures are available with additional details: Figure S1 shows additional XRD patterns for samples before DSC of sintering; Figure S2 is the thermogravimetric and DSC curves for as-synthesized nanoparticles; Figure S3 is the high resolution XPS survey for the nanoparticles before and after the DSC of sintering experiment; Figure S4 shows XRD patterns for nanoparticles calcined at different temperatures during the coarsening experiments; and Figure S5 shows a collection of SEM images of those same coarsened nanoparticles.

Reference

(1) Bruce, P. G.; Scrosati, B.; Tarascon, J. M. Nanomaterials for Rechargeable Lithium Batteries. *Angew. Chemie - Int. Ed.* **2008**, *47* (16), 2930–2946. https://doi.org/10.1002/anie.200702505.

(2) Okubo, M.; Mizuno, Y.; Yamada, H.; Kim, J.; Hosono, E.; Zhou, H.; Kudo, T.; Honma, I. Fast Li-Ion Insertion into Nanosized LiMn2O4 without Domain Boundaries. **2010**, *4* (2), 741–752.

(3) Lu, J.; Chen, Z.; Ma, Z.; Pan, F.; Curtiss, L. A.; Amine, K. The Role of Nanotechnology in the Development of Battery Materials for Electric Vehicles. *Nat. Nanotechnol.* **2016**, *11*, 1031-1038. https://doi.org/10.1038/nnano.2016.207.

(4) Ye, S. H.; Lv, J. Y.; Gao, X. P.; Wu, F.; Song, D. Y. Synthesis and Electrochemical Properties of LiMn2O4 Spinel Phase with Nanostructure. *Electrochim. Acta* **2004**, *49* (9–10), 1623–1628. https://doi.org/10.1016/j.electacta.2003.12.001.

(5) Chen, Y.; Xie, K.; Pan, Y.; Zheng, C. Nano-Sized LiMn2O4 Spinel Cathode Materials Exhibiting High Rate Discharge Capability for Lithium-Ion Batteries. *J. Power Sources* **2011**, *196* (15), 6493–6497. https://doi.org/10.1016/j.jpowsour.2011.03.081.

(6) Itou, Y.; Ukyo, Y. Performance of LiNiCoO2 Materials for Advanced Lithium-Ion Batteries. *J. Power Sources* **2005**, *146* (1–2), 39–44. https://doi.org/10.1016/j.jpowsour.2005.03.091.

(7) Nitta, N.; Wu, F.; Lee, J. T.; Yushin, G. Li-Ion Battery Materials: Present and Future. *Mater. Today* **2015**, *18* (5), 252–264. https://doi.org/10.1016/j.mattod.2014.10.040.

(8) Shin, Y.; Manthiram, A. Microstrain and Capacity Fade in Spinel Manganese Oxides. *Electrochem. Solid-State Lett.* **2002**, *5* (3), 3–6. https://doi.org/10.1149/1.1450063.

(9) Liu, H.; Wolf, M.; Karki, K.; Yu, Y. S.; Stach, E. A.; Cabana, J.; Chapman, K. W.; Chupas, P. J. Intergranular Cracking as a Major Cause of Long-Term Capacity Fading of Layered Cathodes. *Nano Lett.* **2017**, *17* (6), 3452–3457. https://doi.org/10.1021/acs.nanolett.7b00379.

(10) Liu, Q.; Wang, S.; Tan, H.; Yang, Z.; Zeng, J. Preparation and Doping Mode of Doped LiMn2O4 for Li-Ion Batteries. *Energies* **2013**, *6* (3), 1718–1730. https://doi.org/10.3390/en6031718.

(11) Mughal, M. Z.; Moscatelli, R.; Amanieu, H. Y.; Sebastiani, M. Effect of Lithiation on Micro-Scale Fracture Toughness of LixMn2O4 Cathode. *Scr. Mater.* **2016**, *116*, 62–66. https://doi.org/10.1016/j.scriptamat.2016.01.023.

(12) Watanabe, S.; Kinoshita, M.; Hosokawa, T.; Morigaki, K.; Nakura, K. Capacity Fade of LiAlyNi1-x-YCoxO 2 Cathode for Lithium-Ion Batteries during Accelerated Calendar and Cycle Life Tests (Surface Analysis of LiAlyNi1-x-YCo XO2 Cathode after Cycle Tests in Restricted Depth of Discharge Ranges). *J. Power Sources* **2014**, *258*, 210–217. https://doi.org/10.1016/j.jpowsour.2014.02.018.

(13) Navrotsky, A.; Ma, C.; Lilova, K.; Birkner, N. Nanophase Transition Metal Oxides Show Large Thermodynamically Driven Shifts in Oxidation-Reduction Equilibria. *Science (80-.).* **2010**, *330* (6001), 199–201. https://doi.org/10.1126/science.1195875.

(14) Conner, C. L.; Faber, K. T. Segregant-Enhanced Fracture in Magnesium Oxide. *J. Mater. Sci.* **1990**, *25* (6), 2737–2742. https://doi.org/10.1007/BF00584873.

(15) Castro, R. H. R.; Gouvêa, D. Sintering and Nanostability: The Thermodynamic Perspective. *J. Am. Ceram. Soc.* **2016**, *99* (4), 1105–1121. https://doi.org/10.1111/jace.14176.

(16) Hammer, B.; Nørskov, J. K. Theoretical Surface Science and Catalysis—Calculations and Concepts. *Adv. Catal.* **2000**, *45* (C), 71–129. https://doi.org/10.1016/S0360-0564(02)45013-4.

(17) Kang, S.-J. L. *Sintering: Densification, Grain Growth, and Microstructure*; Elsevier: Burlington, MA, 2005, 6-12.

(18) Carter, C. B.; Norton, M. G. *Ceramic Materials*; Springer US: New York, NY, 2013, 253-275. https://doi.org/10.1007/978-1-4614-3523-5.

(19) Sharma, G.; Nakajima, K.; Muche, D. N. F.; Castro, R. H. R. The Influence of Dopants on the Surface Enthalpy of Yttrium Aluminum Garnet (YAG). *Thermochim. Acta* **2020**, *683* (November 2019), 178471. https://doi.org/10.1016/j.tca.2019.178471.

(20) Chang, C. H.; Rufner, J. F.; Benthem, K. Van; Castro, R. H. R. Design of Desintering in Tin Dioxide Nanoparticles. *Chem. Mater.* **2013**, *25* (21), 4262–4268. https://doi.org/10.1021/cm402330u.

(21) Li, H.; Souza, F. L.; Castro, R. H. R. Kinetic and Thermodynamic Effects of Manganese as a Densification Aid in Yttria-Stabilized Zirconia. *J. Eur. Ceram. Soc.* **2018**, *38* (4), 1750–1759. https://doi.org/10.1016/j.jeurceramsoc.2017.10.041.

(22) Peng, H.; Jian, Z.; Liu, F. Review of Thermo-kinetic Correlation during Grain Growth in Nanocrystalline Materials. *Int. J. Ceram. Eng. Sci.* **2020**, *2* (2), 49–65. https://doi.org/10.1002/ces2.10040.

(23) Castro, R. H. R.; Wang, B. The Hidden Effect of Interface Energies in the Polymorphic Stability of Nanocrystalline Titanium Dioxide. *J. Am. Ceram. Soc.* **2011**, *94* (3), 918–924. https://doi.org/10.1111/j.1551-2916.2010.04164.x.

(24) Bedin, K. C.; Freitas, A. L. M.; Tofanello, A.; Rodríguez-Gutiérrez, I.; Souza, F. L. Revealing the Synergy of Sn Insertion in Hematite for Next-Generation Solar Water Splitting Nanoceramics. *Int. J. Ceram. Eng. Sci.* **2020**, *2* (5), 204–227. https://doi.org/https://doi.org/10.1002/ces2.10062.

(25) Hasan, M. M.; Dey, S.; Nafsin, N.; Mardinly, J.; Dholabhai, P. P.; Uberuaga, B. P.; Castro, R. H. R. Improving the Thermodynamic Stability of Aluminate Spinel Nanoparticles with Rare Earths. *Chem. Mater.* **2016**, *28* (14), 5163–5171. https://doi.org/10.1021/acs.chemmater.6b02577.

(26) Zhang, H.; Banfield, J. F. Structural Characteristics and Mechanical and Thermodynamic Properties of Nanocrystalline TiO2. *Chem. Rev.* **2014**, *114* (19), 9613–9644. https://doi.org/10.1021/cr500072j.

(27) Weissmuller, J. Alloy Effects in Nanostructures. *Nanostructured Mater.* **1993**, *3* (2), 261–272.

(28) Kirchheim, R. Reducing Grain Boundary, Dislocation Line and Vacancy Formation Energies by Solute Segregation. I. Theoretical Background. *Acta Mater.* **2007**, *55* (15), 5129–5138. https://doi.org/10.1016/j.actamat.2007.05.047.

(29) Kirchheim, R. Reducing Grain Boundary, Dislocation Line and Vacancy Formation Energies by Solute Segregation. II. Experimental Evidence and Consequences. *Acta Mater.* **2007**, *55* (15), 5139–5148. https://doi.org/10.1016/j.actamat.2007.05.033.

(30) Benedek, R.; Thackeray, M. M. Simulation of the Surface Structure of Lithium Manganese Oxide Spinel. *Phys. Rev. B - Condens. Matter Mater. Phys.* **2011**, *83* (19), 1–8. https://doi.org/10.1103/PhysRevB.83.195439.

(31) Karim, A.; Fosse, S.; Persson, K. A. Surface Structure and Equilibrium Particle Shape of the LiMn 2O4 Spinel from First-Principles Calculations. *Phys. Rev. B - Condens. Matter Mater. Phys.* **2013**, *87* (7), 25–28. https://doi.org/10.1103/PhysRevB.87.075322.

(32) Kim, S.; Aykol, M.; Wolverton, C. Surface Phase Diagram and Stability of (001) and (111) LiM N2 O4 Spinel Oxides. *Phys. Rev. B - Condens. Matter Mater. Phys.* **2015**, *92* (11), 7–10. https://doi.org/10.1103/PhysRevB.92.115411.

(33) Maram, P. S.; Costa, G. C. C.; Navrotsky, A. Experimental Confirmation of Low Surface Energy in LiCoO2 and Implications for Lithium Battery Electrodes. *Angewandte Chemie - International Edition*. 2013, pp 12139–12142. https://doi.org/10.1002/anie.201305375.

(34) Ryu, H.-H.; Park, N.-Y.; Seo, J. H.; Yu, Y.-S.; Sharma, M.; Mücke, R.; Kaghazchi, P.; Yoon, C. S.; Sun, Y.-K. A Highly Stabilized Ni-Rich NCA Cathode for High-Energy Lithium-Ion Batteries. *Mater. Today* **2020**, *36*, 73–82. https://doi.org/https://doi.org/10.1016/j.mattod.2020.01.019.

(35) Zhang, C.; Wang, K.; Liu, C.; Nan, X.; Fu, H.; Ma, W.; Li, Z.; Cao, G. Effects of High Surface Energy on Lithium-Ion Intercalation Properties of Ni-Doped Li3VO4. *NPG Asia Mater.* **2016**, *8* (7), 1–7. https://doi.org/10.1038/am.2016.95.

(36) Warburton, R. E.; Iddir, H.; Curtiss, L. A.; Greeley, J. Thermodynamic Stability of Low- and High-Index Spinel LiMn2O4 Surface Terminations. *ACS Appl. Mater. Interfaces* **2016**, *8* (17), 11108–11121. https://doi.org/10.1021/acsami.6b01069.

(37) Hasan, M. M.; Dholabhai, P. P.; Castro, R. H. R.; Uberuaga, B. P. Stabilization of MgAl2O4 Spinel Surfaces via Doping. *Surf. Sci.* **2016**, *649*, 138–145. https://doi.org/10.1016/j.susc.2016.01.028.

(38) Hasan, M. M.; Dholabhai, P. P.; Dey, S.; Uberuaga, B. P.; Castro, R. H. R. Reduced Grain Boundary Energies in Rare-Earth Doped MgAl2O4 Spinel and Consequent Grain Growth Inhibition. *J. Eur. Ceram. Soc.* **2017**, *37* (13), 4043–4050. https://doi.org/10.1016/j.jeurceramsoc.2017.04.073.

(39) Sharifi-Asl, S.; Yurkiv, V.; Gutierrez, A.; Cheng, M.; Balasubramanian, M.; Mashayek, F.; Croy, J.; Shahbazian-Yassar, R. Revealing Grain-Boundary-Induced Degradation Mechanisms in Li-Rich Cathode Materials. *Nano Lett.* **2020**, *20* (2), 1208–1217. https://doi.org/10.1021/acs.nanolett.9b04620.

(40) Bokov, A.; Zhang, S.; Feng, L.; Dillon, S. J.; Faller, R.; Castro, R. H. R. Energetic Design of Grain Boundary Networks for Toughening of Nanocrystalline Oxides. *J. Eur. Ceram.*

Soc. **2018**, *38* (12), 4260–4267. https://doi.org/10.1016/j.jeurceramsoc.2018.05.007.

(41) Ram, P.; Gören, A.; Ferdov, S.; Silva, M. M.; Singhal, R.; Costa, C. M.; Sharma, R. K.; Lanceros-Méndez, S. Improved Performance of Rare Earth Doped LiMn2O4 Cathodes for Lithium-Ion Battery Applications. *New J. Chem.* **2016**, *40* (7), 6244–6252. https://doi.org/10.1039/c6nj00198j.

(42) Ouyang, C. Y.; Zeng, X. M.; Šljivancanin, Ž.; Baldereschi, A. Oxidation States of Mn Atoms at Clean and Al2O 3-Covered LiMn2O4(001) Surfaces. *J. Phys. Chem. C* **2010**, *114* (10), 4756–4759. https://doi.org/10.1021/jp911746g.

(43) Bhuvaneswari, S.; Varadaraju, U. V.; Gopalan, R.; Prakash, R. Structural Stability and Superior Electrochemical Performance of Sc-Doped LiMn 2 O 4 Spinel as Cathode for Lithium Ion Batteries. *Electrochim. Acta* **2019**, *301*, 342–351. https://doi.org/10.1016/j.electacta.2019.01.174.

(44) Mueller, R.; Mädler, L.; Pratsinis, S. E. Nanoparticle Synthesis at High Production Rates by Flame Spray Pyrolysis. *Chem. Eng. Sci.* **2003**, *58* (10), 1969–1976. https://doi.org/10.1016/S0009-2509(03)00022-8.

(45) Teoh, W. Y.; Amal, R.; Mädler, L. Flame Spray Pyrolysis: An Enabling Technology for Nanoparticles Design and Fabrication. *Nanoscale* **2010**, *2* (8), 1324–1347. https://doi.org/10.1039/c0nr00017e.

(46) Yi, J. H.; Kim, J. H.; Koo, H. Y.; Ko, Y. N.; Kang, Y. C.; Lee, J. H. Nanosized LiMn2O4 Powders Prepared by Flame Spray Pyrolysis from Aqueous Solution. *J. Power Sources* **2011**, *196* (5), 2858–2862. https://doi.org/10.1016/j.jpowsour.2010.11.038.

(47) Ernst, F. O.; Kammler, H. K.; Roessler, A.; Pratsinis, S. E.; Stark, W. J.; Ufheil, J.; Novák, P. Electrochemically Active Flame-Made Nanosized Spinels: LiMn2O4,

Li4Ti5O12 and LiFe5O8. *Mater. Chem. Phys.* **2007**, *101* (2–3), 372–378. https://doi.org/10.1016/j.matchemphys.2006.06.014.

(48) Sorvali, M.; Nikka, M.; Juuti, P.; Honkanen, M.; Salminen, T.; Hyvärinen, L.; Mäkelä, J. M. Controlling the Phase of Iron Oxide Nanoparticles Fabricated from Iron(III) Nitrate by Liquid Flame Spray. *Int. J. Ceram. Eng. Sci.* **2019**, *1* (4), 194–205. https://doi.org/https://doi.org/10.1002/ces2.10025.

(49) Maeda, S.; Iwabuchi, S.; Shiojiri, M. Differential Scanning Calorimetry of the Coalescence Growth of Fine Smoke Particles. *Jpn. J. Appl. Phys.* **1984**, *23* (7R), 830–835. https://doi.org/10.1143/JJAP.23.830.

(50) Hayun, S.; Ushakov, S. V.; Navrotsky, A. Direct Measurement of Surface Energy of CeO2 by Differential Scanning Calorimetry. *J. Am. Ceram. Soc.* **2011**, *94* (11), 3679–3682. https://doi.org/10.1111/j.1551-2916.2011.04843.x.

(51) Terwllliger, C. D.; Chiang, Y. -M. Measurements of Excess Enthalpy in Ultrafine-Grained Titanium Dioxide. *J. Am. Ceram. Soc.* **1995**, *78* (8), 2045–2055. https://doi.org/10.1111/j.1151-2916.1995.tb08616.x.

(52) Castro, R. H. R.; Tŏrres, R. B.; Pereira, G. J.; Gouvĕa, D. Interface Energy Measurement of MgO and ZnO: Understanding the Thermodynamic Stability of Nanoparticles. *Chem. Mater.* **2010**, *22* (8), 2502–2509. https://doi.org/10.1021/cm903404u.

(53) Muche, D. N. F.; Marple, M. A. T.; Sen, S.; Castro, R. H. R. Grain Boundary Energy, Disordering Energy and Grain Growth Kinetics in Nanocrystalline MgAl2O4 Spinel. *Acta Mater.* **2018**, *149*, 302–311. https://doi.org/10.1016/j.actamat.2018.02.052.

(54) Mendelson, M. I. Average Grain Size in Polycrystalline Ceramics. *J. Am. Ceram. Soc.* **1969**, *52* (8), 443–446. https://doi.org/10.1111/j.1151-2916.1969.tb11975.x.

(55) Hiemstra, T. Formation, Stability, and Solubility of Metal Oxide Nanoparticles: Surface Entropy, Enthalpy, and Free Energy of Ferrihydrite. *Geochim. Cosmochim. Acta* **2015**, *158*, 179–198. https://doi.org/https://doi.org/10.1016/j.gca.2015.02.032.

(56) Wang, L.; Vu, K.; Navrotsky, A.; Stevens, R.; Woodfield, B. F.; Boerio-Goates, J. Calorimetric Study: Surface Energetics and the Magnetic Transition in Nanocrystalline CoO. *Chem. Mater.* **2004**, *16* (25), 5394–5400. https://doi.org/10.1021/cm049040i.

(57) McCormack, S. J.; Navrotsky, A. Thermodynamics of High Entropy Oxides. *Acta Mater.* **2021**, *202*, 1–21. https://doi.org/https://doi.org/10.1016/j.actamat.2020.10.043.

(58) Ushakov, S. V.; Navrotsky, A. Direct Measurements of Water Adsorption Enthalpy on Hafnia and Zirconia. *Appl. Phys. Lett.* **2005**, *87* (16), 1–3. https://doi.org/10.1063/1.2108113.

(59) Hayun, S.; Shvareva, T. Y.; Navrotsky, A. Nanoceria-Energetics of Surfaces, Interfaces and Water Adsorption. *J. Am. Ceram. Soc.* **2011**, *94* (11), 3992–3999. https://doi.org/10.1111/j.1551-2916.2011.04648.x.

(60) Drazin, J. W.; Castro, R. H. R. Water Adsorption Microcalorimetry Model: Deciphering Surface Energies and Water Chemical Potentials of Nanocrystalline Oxides. *J. Phys. Chem. C* **2014**, *118* (19), 10131–10142. https://doi.org/10.1021/jp5016356.

(61) Castro, R. H. R.; Quach, D. V. Analysis of Anhydrous and Hydrated Surface Energies of Gamma-Al 2O3 by Water Adsorption Microcalorimetry. *J. Phys. Chem. C* **2012**, *116* (46), 24726−24733. https://doi.org/10.1021/jp309319j.

(62) Drazin, J. W.; Castro, R. H. R. Phase Stability in Nanocrystals: A Predictive Diagram for Yttria-Zirconia. *J. Am. Ceram. Soc.* **2015**, *98* (4), 1377–1384. https://doi.org/10.1111/jace.13504.

(63) Muche, D. N. F.; Souza, F. L.; Castro, R. H. R. New Ultrasonic Assisted Co-Precipitation for High Surface Area Oxide Based Nanostructured Materials. *React. Chem. Eng.* **2018**, *3* (3), 244–250. https://doi.org/10.1039/c7re00183e.

(64) Yamada, A. Synthesis and Structural Aspects of LiMn[Sub 2]O[Sub 4±δ] as a Cathode for Rechargeable Lithium Batteries. *J. Electrochem. Soc.* **1995**, *142* (7), 2149. https://doi.org/10.1149/1.2044266.

(65) Fritsch, S.; Navrotsky, A. Thermodynamic Properties of Manganese Oxides. *J. Am. Ceram. Soc.* **1996**, *79* (7), 1761–1768.

(66) Ramana, C. V.; Massot, M.; Julien, C. M. XPS and Raman Spectroscopic Characterization of LiMn2O 4 Spinels. *Surf. Interface Anal.* **2005**, *37* (4), 412–416. https://doi.org/10.1002/sia.2022.

(67) Marchini, F.; Rubi, D.; Del Pozo, M.; Williams, F. J.; Calvo, E. J. Surface Chemistry and Lithium-Ion Exchange in LiMn2O4 for the Electrochemical Selective Extraction of LiCl from Natural Salt Lake Brines. *J. Phys. Chem. C* **2016**, *120* (29), 15875–15883. https://doi.org/10.1021/acs.jpcc.5b11722.

(68) Tang, D.; Ben, L.; Sun, Y.; Chen, B.; Yang, Z.; Gu, L.; Huang, X. Electrochemical Behavior and Surface Structural Change of LiMn 2O4 Charged to 5.1 V. *J. Mater. Chem. A* **2014**, *2* (35), 14519–14527. https://doi.org/10.1039/c4ta02109f.

(69) Siva Reddy, K.; Gangaja, B.; Nair, S. V.; Santhanagopalan, D. Mn4+ Rich Surface Enabled Elevated Temperature and Full-Cell Cycling Performance of LiMn2O4 Cathode Material. *Electrochim. Acta* **2017**, *250*, 359–367. https://doi.org/10.1016/j.electacta.2017.08.054.

(70) Nakajima, K.; Li, H.; Shlesinger, N.; Rodrigues Neto, J. B.; Castro, R. H. R. Low-

Temperature Sintering of Magnesium Aluminate Spinel Doped with Manganese: Thermodynamic and Kinetic Aspects. *J. Am. Ceram. Soc.* **2020**, *103* (8), 4167–4177. https://doi.org/10.1111/jace.17162.

(71) Castro, R. H. R.; Benthem, K. van. *Sintering- Mechanism of Convention Nanodensification and Field Assisted Process*; Springer: Berlin, Germany, 2013, 57-95. https://doi.org/10.1007/978-3-642-31009-6.

(72) Bae, I.-J.; Baik, S. Abnormal Grain Growth of Alumina. *J. Am. Ceram. Soc.* **2005**, *80* (5), 1149–1156. https://doi.org/10.1111/j.1151-2916.1997.tb02957.x.

(73) Lee, J. W.; Kim, J. Il; Min, S. H. Highly Crystalline Lithium-Manganese Spinel Prepared by a Hydrothermal Process with Co-Solvent. *J. Power Sources* **2011**, *196* (3), 1488–1493. https://doi.org/10.1016/j.jpowsour.2010.08.083.

(74) Saylor, D. M.; Dasher, B. El; Pang, Y.; Miller, H. M.; Wynblatt, P.; Rollett, A. D.; Rohrer, G. S. Habits of Grains in Dense Polycrystalline Solids. *J. Am. Ceram. Soc.* **2004**, *87* (4), 724–726. https://doi.org/10.1111/j.1551-2916.2004.00724.x.

(75) Miers, H. A. *Mineralogy: An Introduction to the Scientifict Study of Minerals*, Second edi.; Macmilland and Co., Ltd.: London, 1929, 382-387.

(76) Pereira, G. J.; Bolis, K.; Muche, D. N. F.; Gouvêa, D.; Castro, R. H. R. Direct Measurement of Interface Energies of Magnesium Aluminate Spinel and a Brief Sintering Analysis. *J. Eur. Ceram. Soc.* **2017**, *37* (13), 4051–4058. https://doi.org/10.1016/j.jeurceramsoc.2017.05.035.

(77) Yang, C.; Zhu, W.; Sen, S.; Castro, R. H. R. Site Inversion Induces Thermodynamic Stability against Coarsening in Zinc Aluminate Spinel. *J. Phys. Chem. C* **2019**, *123* (14), 8818–8826. https://doi.org/10.1021/acs.jpcc.8b11378.

(78) Kramer, D.; Ceder, G. Tailoring the Morphology of LiCoO2: A First Principles Study. *Chem. Mater.* **2009**, *21* (16), 3799–3809. https://doi.org/10.1021/cm9008943.

(79) Persson, K. A.; Waldwick, B.; Lazic, P.; Ceder, G. Prediction of Solid-Aqueous Equilibria: Scheme to Combine First-Principles Calculations of Solids with Experimental Aqueous States. *Phys. Rev. B - Condens. Matter Mater. Phys.* **2012**, *85* (23), 1–12. https://doi.org/10.1103/PhysRevB.85.235438.

(80) Birkner, N.; Navrotsky, A. Thermodynamics of Manganese Oxides: Effects of Particle Size and Hydration on Oxidation-Reduction Equilibria among Hausmannite, Bixbyite, and Pyrolusite. *Am. Mineral.* **2012**, *97* (8–9), 1291–1298. https://doi.org/10.2138/am.2012.3982.

(81) Schwab, C.; Höweling, A.; Windmüller, A.; Gonzalez-Julian, J.; Möller, S.; Binder, J. R.; Uhlenbruck, S.; Guillon, O.; Martin, M. Bulk and Grain Boundary Li-Diffusion in Dense LiMn2O4 Pellets by Means of Isotope Exchange and ToF-SIMS Analysis. *Phys. Chem. Chem. Phys.* **2019**, *21* (47), 26066–26076. https://doi.org/10.1039/c9cp05128g.

(82) Avila-Paredes, H. J.; Kim, S. The Effect of Segregated Transition Metal Ions on the Grain Boundary Resistivity of Gadolinium Doped Ceria: Alteration of the Space Charge Potential. *Solid State Ionics* **2006**, *177* (35–36), 3075–3080. https://doi.org/10.1016/j.ssi.2006.08.017.

(83) Seah, M. P. Grain Boundary Segregation. *J. Phys. F Met. Phys.* **1980**, *10* (6), 1043–1064. https://doi.org/10.1088/0305-4608/10/6/006.

(84) Zhang, P.; Navrotsky, A.; Guo, B.; Kennedy, I.; Clark, A. N.; Lesher, C.; Liu, Q. Energetics of Cubic and Monoclinic Yttrium Oxide Polymorphs: Phase Transitions, Surface Enthalpies, and Stability at the Nanoscale. *J. Phys. Chem. C* **2008**, *112* (4), 932–

938. https://doi.org/10.1021/jp7102337.

(85) Pender, J. P.; Jha, G.; Youn, D. H.; Ziegler, J. M.; Andoni, I.; Choi, E. J.; Heller, A.; Dunn, B. S.; Weiss, P. S.; Penner, R. M.; Mullins, C. B. Electrode Degradation in Lithium-Ion Batteries. *ACS Nano* **2020**, *14* (2), 1243–1295. https://doi.org/10.1021/acsnano.9b04365.

(86) Li, H.; Dey, S.; Castro, R. H. R. Kinetics and Thermodynamics of Densification and Grain Growth: Insights from Lanthanum Doped Zirconia. *Acta Mater.* **2018**, *150*, 394–402. https://doi.org/10.1016/j.actamat.2018.03.033.

(87) Cupid, D. M.; Reif, A.; Seifert, H. J. Enthalpy of Formation of Li1+xMn2-XO4 (0 < x < 0.1) Spinel Phases. *Thermochim. Acta* **2015**, *599*, 35–41. https://doi.org/10.1016/j.tca.2014.11.003.

(88) Wang, M.; Navrotsky, A. Thermochemistry of Li1+xMn2-XO4 (0≤x≤1/3) Spinel. *J. Solid State Chem.* **2005**, *178* (4), 1182–1189. https://doi.org/10.1016/j.jssc.2004.12.007.

(89) Amos, C. D.; Roldan, M. A.; Varela, M.; Goodenough, J. B.; Ferreira, P. J. Revealing the Reconstructed Surface of Li[Mn 2]O 4. **2016**, 2–9. https://doi.org/10.1021/acs.nanolett.5b03926.

(90) Hunter, J. C. Preparation of a New Crystal Form of Manganese Dioxide : λ-MnO2. *J. Solid State Chem.* **1981**, *39*, 142–147.

(91) Idemoto, Y.; Ogawa, S.; Uemura, Y.; Koura, N. Thermodynamic Stability and Cathode Performance of Li1+xMn2-XO4 as a Cathode Active Material for Lithium Secondary Battery. *J. Ceram. Soc. Japan* **2000**, *108* (9), 848–853. https://doi.org/10.2109/jcersj.108.1261_848.

(92) Ishida, N.; Tamura, N.; Kitamura, N.; Idemoto, Y. Crystal and Electronic Structure

Analysis and Thermodynamic Stabilities for Electrochemically or Chemically Delithiated Li1.2-XMn0.54Ni0.13Co0.13O2. *J. Power Sources* **2016**, *319*, 255–261. https://doi.org/10.1016/j.jpowsour.2016.04.060.

(93) Idemoto, Y.; Horiko, K.; Ui, K.; Koura, N. Thermodynamic Stability and Crystal Structure Dependence of Li Content for LixMn2-YMyO4(M=Mg, Al, Cr, Mn) as a Cathode Active Material for Li Secondary Battery. *Electrochemistry* **2004**, *72* (10), 680–687.

ToC